

A Study of the Point Spread Function in SDSS Images

B. Xin¹, Ž. Ivezić², R. H. Lupton³, J. R. Peterson⁴, P. Yoachim², R. L. Jones², C. Claver¹,
and G. Angeli^{1*}

¹*Large Synoptic Survey Telescope, Tucson, AZ 85719*

²*Department of Astronomy, University of Washington, Seattle, WA 98195*

³*Department of Astrophysical Sciences, Princeton University, Princeton, NJ 08544*

⁴*Department of Physics and Astronomy, Purdue University, West Lafayette, IN 47907*

ABSTRACT

We use SDSS imaging data in *ugriz* passbands to study the shape of point spread function (PSF) profile and the variation of its width with wavelength and time. We find that the PSF profile is well described by theoretical predictions based on von Kármán’s turbulence theory. The observed profile can be parametrized by only two parameters, the profile’s FWHM (full width at half maximum) and a normalization of the contribution of an empirically determined instrumental PSF. The profile shape is very similar to the “double gaussian plus power-law wing” decomposition used by SDSS image processing pipeline, but here it is modeled with two free model parameters, rather than six as in SDSS pipeline. The FWHM variation with wavelength follows the λ^α power law, where $\alpha \approx -0.3$, and is correlated with the FWHM itself. This behavior is much better described by von Kármán’s turbulence theory with the outer scale parameter in the range 10–30 m, than by the Kolmogorov’s turbulence theory. We also measure the temporal and angular structure functions for FWHM and compare them to simulations and existing measurements. The angular structure function saturates at scales beyond 0.5–1.0 degree. The power spectrum of the temporal behavior is found to be broadly consistent with a damped random walk model with characteristic timescale in the range $\sim 10 - 30$ minutes, though data show a shallower high-frequency behavior. The latter is well fit by a single power law with index in the range -1.5 to -1.0 . A hybrid model is likely needed to fully capture both the low-frequency and high-frequency behavior of the temporal variations of atmospheric seeing.

*Current address: Giant Magellan Telescope Organization, Pasadena, CA 91107

Subject headings: SDSS — imaging point spread function — turbulence

1. Introduction

The atmospheric seeing, the point-spread function (PSF) due to atmospheric turbulence, plays a major role in ground-based astronomy (Roddier 1981). An adequate description of the PSF is critical for photometry, star-galaxy separation, and for unbiased measures of the shapes of nonstellar objects (Lupton et al. 2001). In addition, better understanding of the PSF temporal variation can lead to improved seeing forecasts; for example, such forecasts are considered in the optimization of LSST observing strategy (Ivezić et al. 2008).

Seeing varies with the wavelength of observation, and it also varies with time, on time scales ranging from minutes to years. These variations, as well as the radial seeing (PSF) profile, can be understood as manifestations of atmospheric instabilities due to turbulent layers. Although turbulence is a complex physical phenomenon, the basic properties of the atmospheric seeing can be predicted from first principles (Racine 2009). The von Kármán turbulence theory, an extension of the Komogorov theory that introduces a finite size for turbulent eddies (the so-called outer scale parameter), quantitatively predicts the seeing profile and the variation of seeing with wavelength (Borgnino 1990; Ziad et al. 2000). Therefore, seeing measurements can be used to test the theory and estimate the relevant physical parameters.

An unprecedentedly large high-quality database of seeing measurements was delivered by the Sloan Digital Sky Survey (SDSS, York et al. 2000), a large-area multi-bandpass digital sky survey. The SDSS delivered homogeneous and deep ($r \lesssim 22.5$) photometry in five bandpasses (u , g , r , i , and z , with effective wavelengths of 3551, 4686, 6166, 7480, and 8932 Å), accurate to about 0.02 mag for unresolved sources not limited by photon statistics (Sesar et al. 2007). Astrometric positions are accurate to better than 0.1 arcsec per coordinate for sources with $r < 20.5$ (Pier et al. 2003), and the morphological information from the images allows reliable star-galaxy separation to $r < 21.5$ (Lupton et al. 2002).

The SDSS camera (Gunn et al. 1998) used drift-scanning observing mode (scanning along great circles at the sidereal rate) and detected objects in the order r - i - u - z - g , with detections in two successive bands separated in time by 72 s. Each of the six camera columns produces a 13.5 arcmin wide scan; the scans are split into fields 9.0 arcmin long, corresponding to 36 seconds of time (the exposure time is 54.1 seconds because the sensor size is 2k by 2k pixels, with 0.396 arcsec per pixel). The point-spread function (PSF) is estimated for each field and in each bandpass - there are about 148 seeing estimates for each square degree of scanned sky. As a result, the SDSS measurements can be used to explore the seeing

dependence on time (on time scales from 1 minute to 10 hours) and wavelength (from the UV to the near-IR), as well as its angular correlation on the sky on scales from arcminutes to about 2.5 degrees. Thanks to large dynamic range for stellar brightness, the PSF can be traced to large radii (~ 30 arcsec) and compared to seeing profiles predicted by turbulence theories¹.

The SDSS seeing measurements represent an excellent database that has not been systematically explored yet. Here we utilize about a million SDSS seeing estimates to study the seeing profile and its behavior as a function of time and wavelength, and compare our results to theoretical expectations. The outline of this paper is as follows. In §2, we give a brief description of the observations and the data used in analysis. We describe the PSF profile analysis, including estimation method for the full-width-at-half-maximum (FWHM) seeing parameter, in §3. In §4, we analyse the dependence of FWHM on wavelength, and its angular and temporal structure functions. We present and discuss our conclusions in §5.

2. Data Overview

We describe here the SDSS dataset and seeing estimates used in this work. The selected subset of data, the so-called Stripe 82, represents about one third of all SDSS imaging data.

2.1. Stripe 82 dataset

The equatorial Stripe 82 region ($22^h24^m < \text{R.A.} < 04^h08^m$, $-1.27^\circ < \text{Dec} < +1.27^\circ$, about 290 deg^2) from the southern Galactic cap ($-64^\circ < b < -20^\circ$) has been repeatedly imaged (of the order hundred times) by SDSS to study time-domain phenomena (such as supernovae, asteroids, variable stars, quasar variability). An observing stretch of SDSS imaging data is called a “run”. Often there is only a single run for a given observing night, though sometimes there are multiple runs per night. We use here seeing data for 108 runs, with a total of 31,580 fields, obtained between September, 1998 and September 2008). For each field, there 30 seeing estimates (there are 6 camera columns, each with 5 filters; for more details please Gunn et al. 2006). All runs are obtained during the Fall observing season (September to December). Astrometric and photometric aspects of this dataset have

¹For most parts of this paper, we consider the SDSS PSF size same as the seeing, since the PSF is dominated by the atmosphere. But we do keep in mind that the instrument also contributes to the PSF. This is especially important when we analyze the shape of the PSF in the next Section.

been discussed in detail by Ivezić et al. (2007) and Sesar et al. (2007).

2.2. The treatment of seeing in SDSS

Even in the absence of atmospheric inhomogeneities, the SDSS telescope delivers images whose FWHMs vary by up to 15% from one side of a CCD to the other; the worst effects are seen in the chips farthest from the optical axis (Gunn et al. 2006). Moreover, since the atmospheric seeing varies with time, the delivered image quality is a complex two-dimensional function even on the scale of a single frame (for an example of the instantaneous image quality across the imaging camera, see Figure 7 in Stoughton et al. 2002).

The SDSS imaging PSF is modeled heuristically in each band using a Karhunen-Loève (K-L) transform (Lupton et al. 2002). Using stars brighter than roughly 20th magnitude, the PSF images from a series of five frames are expanded into eigenimages and the first three terms are kept (K-L transform is also known as the Principal Component Analysis). The angular variation of the eigencoefficients is fit with polynomials, using data from the frame in question, plus the immediately preceding and following half-frames. The success of this K-L expansion is gauged by comparing PSF photometry based on the modeled K-L PSFs with large-aperture photometry for the same (bright) stars (Stoughton et al. 2002). Parameters that characterize seeing for one field of imaging data are stored in the so-called psField files². The status parameter flag for each frame indicates the success of the K-L decomposition.

In addition to the K-L decomposition, the SDSS processing pipeline computes parameters of the best-fit double Gaussian, evaluated at the center of each frame. The measured PSF profiles are extended to ~ 30 arcsec using observations of bright stars and at such large radii double Gaussian fits underpredict the measured profiles. For this reason, the fits are extended to include the so-called “power-law wings”

$$PSF(r) = \frac{\exp(-\frac{r^2}{2\sigma_1^2}) + b \exp(-\frac{r^2}{2\sigma_2^2}) + p_0 \left(1 + \frac{r^2}{\beta\sigma_P^2}\right)^{-\beta/2}}{1 + b + p_0}. \quad (1)$$

The measured PSFs are thus modeled using 6 free parameters (σ_1 , σ_2 , σ_P , b , p_0 and β), and given that the measured profiles include only up to 10 data points, the fits are usually excellent. The best-fit parameters are reported in psField files.

²https://data.sdss.org/datamodel/files/PHOTO_REDUX/RERUN/RUN/objcs/CAMCOL/psField.html

3. The PSF profile analysis

Since the complex 6-parameter PSF fit given by Eq. (1) was adopted by the SDSS processing pipeline, significant progress has been made in validating the von Kármán model of the atmosphere and measuring the associated outer scale (see, for example, Tokovinin 2002, Boccas 2004, and Martinez et al. 2010). In this section, we describe our much simpler 2-parameter fits to the SDSS PSF profiles using the von Kármán atmosphere model.

Our fitting of each PSF profile is a 2-step process. First we fit the measured PSF profile to a von Kármán PSF, with only one free parameter - the FWHM of the von Kármán profile. The von Kármán PSF profile is generated by creating the atmosphere structure function first, as given by Eq. (18) in Tokovinin (2002), then calculating the PSF through the Optical Transfer Function. The radial profiles of the von Kármán PSF with a few different values of outer scale is shown in Fig. 1. The shape variation due to uncertainty in the outer scale, L_0 , is seen to be small. In this work, we have assumed a fiducial outer scale of 30 meters. The impact of the exact value of L_0 is small, as illustrated in Fig. 1. We note that a fixed value of L_0 induces a small systematic uncertainty in the normalization of the contribution of instrumental PSF, discussed in § 3.1 below.

Ideally, the Fried parameter r_0 would be used as the free parameter in the fit to the von Kármán model. However, that would require us to calculate the special functions and do the Fourier Transform on a large array for each function evaluation. Instead, we opted to generate a single von Kármán PSF template with the FWHM of 1 arcsec. In our one-parameter von Kármán fit, we only stretch or compress the template radially to get the best match with the data, in the least-square sense.

Although the fitted curves agree with the input data points very well, generally much better than the original 6-parameter double-Gaussian fit by SDSS, they do not always describe the PSF tail beyond ~ 15 arcsec radius. This discrepancy is easily understood because it is well known that the PSF tails in the optical bands can be quite different due to the properties of the CCDs. For example, the SDSS i -band PSF has “stronger tails” because of scattering in the CCD. The Si is transparent at long i -band wavelengths so light goes all the way through the chip and is reflected off the solder, and passes back up through the Si. This effect is not visible in the z -band because in this case thick front-side chips are used (in all other bands, thin back-side chips are used).

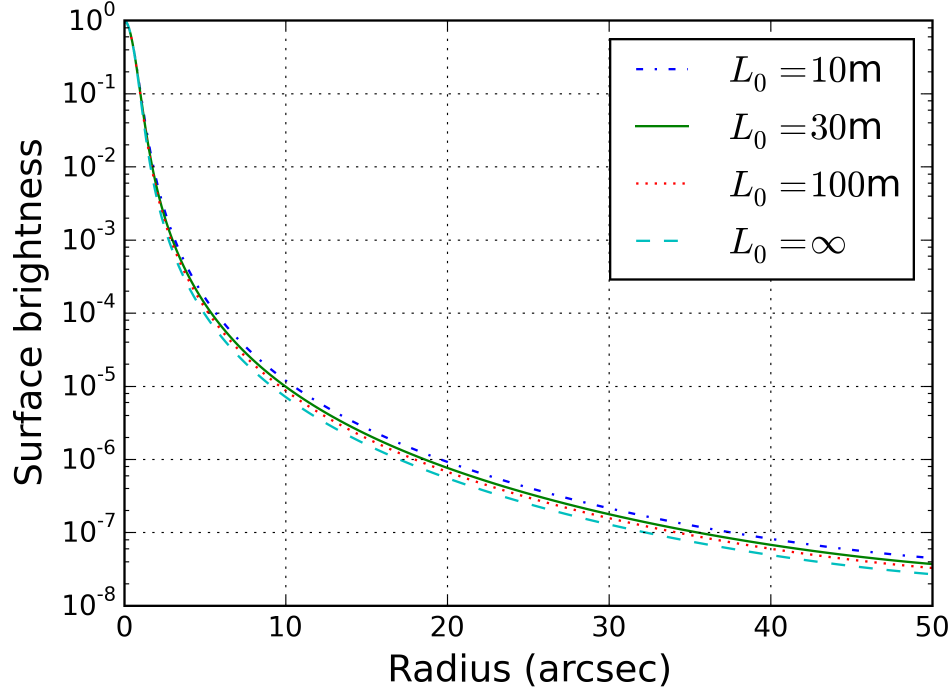


Fig. 1.— PSF radial profiles with the von Kármán model for a few different outer scale (L_0) values. All profiles have FWHM of 1 arcsec, and are normalized to unit peak intensity. The von Kármán model becomes Kolmogorov when $L_0 = \infty$.

3.1. Instrumental PSF

To improve the fit quality at large radii, in the second fitting step we introduce an empirical instrumental PSF, so that the observed PSF can be expressed as a convolution of the atmosphere, represented by the von Kármán, and the instrumental PSF,

$$\text{PSF} = \text{vonK}(\text{FWHM}) \otimes \text{PSF}_{\text{inst}}, \quad (2)$$

where vonK is the von Kármán shape, whose only parameter is its FWHM, and

$$\text{PSF}_{\text{inst}} = \exp\left(-\frac{r^2}{2\sigma^2}\right) + 10^{\eta(ar^2+br+c)}. \quad (3)$$

The standard deviation of the central Gaussian, σ , cannot be too wide because the von Kármán term already well describes the core of the PSF. On the other hand, if σ is close to zero, once the total intensity of the instrumental PSF is normalized to 1, too much widening power would be given to the instrumental PSF tail. We found that $\sigma = 0.1$ arcsec is an acceptable choice for all the fits. Because the shape of the instrumental PSF tail should not

vary with time, the parameters a , b , and c in Eq. (3) are fixed for each band-camera-column combination. Their values come from a one-time fit using the same PSF functions, but with a , b , and c as additional free parameters. We used here run 94, field 11 for these one-time fits, but verified that the results are stable for other choices of run and field. These fits are very slow but need to be done only once. The best-fit values of a , b , and c are listed in Table 1. Although this second fitting step involves a 2-dimensional convolution, there is only one free parameter in the fit: η , the normalization of the instrumental PSF tail. Each two-step PSF fit can be done in a few seconds.

Fig. 2 shows the results of our PSF fits from run 4874. The two-parameter best fits describe the PSF profiles quite well, both in the core and in the tails. There are a total of 108 runs in the SDSS Stripe 82 dataset. Among them, run 4874 is the longest, with 981 fields. In the rest of this paper, whenever we illustrate results from a single run, we always use run 4874 as the fiducial example run.

Table 1: Values for instrumental PSF shape parameters a , b , and c .

		Camera Column					
		1	2	3	4	5	6
u	$a(\times 10^{-3})$	2.2	2.2	1.1	2.2	2.2	2.2
	$b(\times 10^{-1})$	-1.7	-1.7	-7.7	-2.3	-2.3	-2.3
	c	-5.0	-5.0	-6.0	-5.0	-5.0	-5.0
g	$a(\times 10^{-3})$	2.7	2.7	2.2	2.2	2.7	2.7
	$b(\times 10^{-1})$	-1.7	-1.7	-1.7	-1.7	-1.7	-1.7
	c	-5.0	-5.0	-5.0	-5.0	-5.0	-5.0
r	$a(\times 10^{-3})$	2.4	2.4	2.4	2.9	2.2	2.2
	$b(\times 10^{-1})$	-1.6	-1.6	-1.6	-1.6	-1.7	-1.7
	c	-5.0	-5.0	-5.0	-5.0	-5.0	-5.0
i	$a(\times 10^{-3})$	0.7	1.1	0.7	0.7	0.8	0.2
	$b(\times 10^{-1})$	-0.8	-0.9	-0.8	-0.8	-0.9	-0.8
	c	-5.0	-5.0	-5.0	-5.0	-5.0	-5.0
z	$a(\times 10^{-3})$	3.1	-2.2	3.1	2.2	3.1	2.2
	$b(\times 10^{-1})$	-2.0	-1.0	-2.0	-1.5	-2.2	-2.3
	c	-5.0	-5.0	-5.0	-5.0	-5.0	-5.0

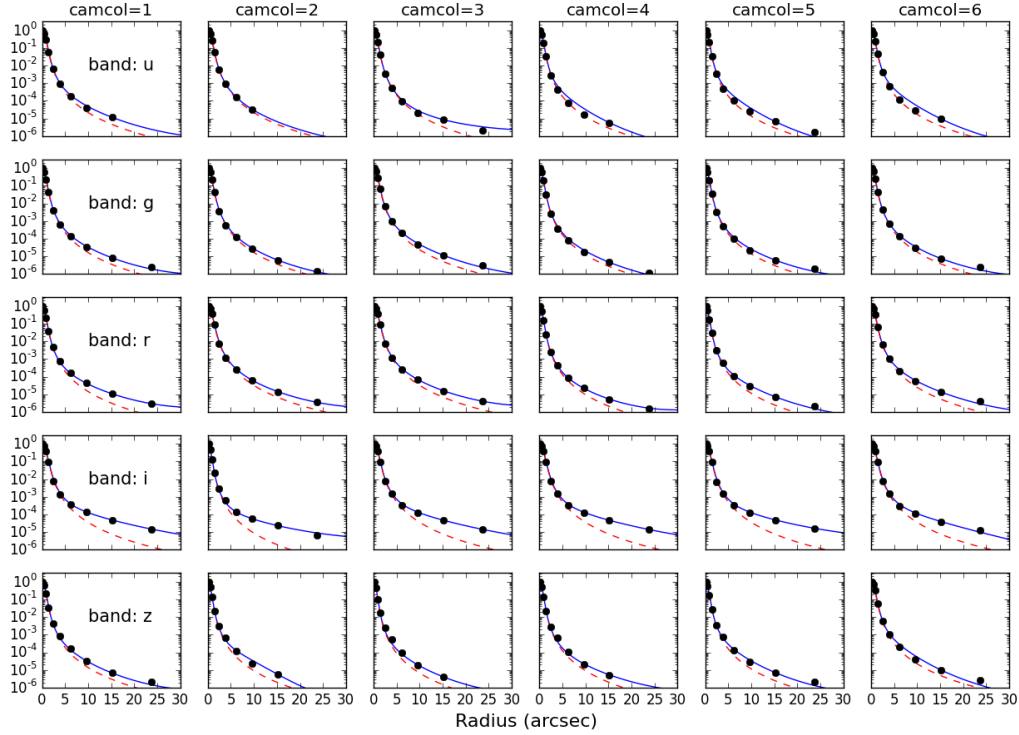


Fig. 2.— Fits to the PSF profiles from run 4874, field 21. Symbols are SDSS data. Red dashed curves are the best one-parameter von Kármán fits. Blue curves are the red curve convolved with the instrumental PSF, where the scaling factor (normalization) for the tail component is allowed to vary. The addition of the instrumental PSF significantly improves the fit quality, especially in the *i*-band. Note that the y-axis is shown on the logarithmic scale.

4. The analysis of FWHM behavior

Given that the observed seeing is by and large described by a single parameter, FWHM, we study three aspects of its variation in detail, as follows.

4.1. The FWHM dependence on wavelength

The Kolmogorov turbulence theory gives a standard formula for the FWHM of a long-exposure seeing-limited PSF in a large telescope,

$$\text{FWHM}^{\text{Kolm}}(\lambda, X) = \frac{0.976\lambda}{r_0(\lambda, X)}. \quad (4)$$

Here λ is the wavelength, X is the airmass, and r_0 is the Fried parameter. We use $\lambda = 500$ nm as the reference wavelength,

$$r_0(\lambda, X) = r_0(500) \left(\frac{\lambda}{500} \right)^{1.2} \frac{1}{X^{0.6}}, \quad (5)$$

where $r_0(500)$ is the r_0 for $\lambda = 500$ nm and $X=1$, and λ is expressed in nm. Substituting Eq. (5) into (4), it is easy to show that

$$\text{FWHM}^{\text{Kolm}} \propto \lambda^{-0.2}. \quad (6)$$

With the von Kármán atmosphere model, the FWHM as in Eq. (4) needs an additional correction factor which is a function of the outer scale L_0 (Tokovinin 2002),

$$\text{FWHM}^{\text{vonK}}(\lambda, X) = \frac{0.976\lambda}{r_0(\lambda, X)} \sqrt{1 - 2.183 \left(\frac{r_0(\lambda, X)}{L_0} \right)^{0.356}}. \quad (7)$$

If power-law approximation is attempted, $\text{FWHM}^{\text{vonK}} \propto \lambda^\alpha$, α becomes a function of L_0 and r_0 at a specified wavelength and airmass, or equivalently, a function of L_0 and $\text{FWHM}^{\text{vonK}}$. For the subsequent analysis, we adopt the r band as the fiducial band (with the effective wavelength of 616.6 nm).

For each run from SDSS Stripe 82 data, and each camera column, we make a least-square fit to all the simultaneous FWHM measurements across the optical bands, to estimate the power-law index α . All FWHM values are multiplied by $1/X^{0.6}$ to correct for the airmass effects. We take into account that the same field number does not correspond to the same time in all filters. The scanning order in the SDSS camera is $r-i-u-z-g$, with the delay between the two successive filters corresponding to 2 fields. That is, if we take the field number F for the r -band, then we need to take FWHM for the i -band from field $F - 2$, for the u -band from $F - 4$, and so on.

Fig. 3 shows such fits for run 4874. All FWHM are normalized using corresponding FWHM in the r -band taken at the same moment in time. Significant deviation from $\alpha = -0.2$, predicted by the Kolmogorov model, can be seen in most bands.

As discussed above, according to the von Kármán atmosphere model, the power index α should be a function of the outer scale L_0 and FWHM. Fig. 4 shows a scatter plot of best-fit α (averaged over six columns) versus the FWHM in the r -band, for all analyzed runs. A correlation between α and the FWHM seems to be present. Similar correlations have been seen in Subaru images and reported by Oya et al. (2016). The data points are overlaid with curves predicted by the von Kármán model, with L_0 varying from 2 m to infinity. The

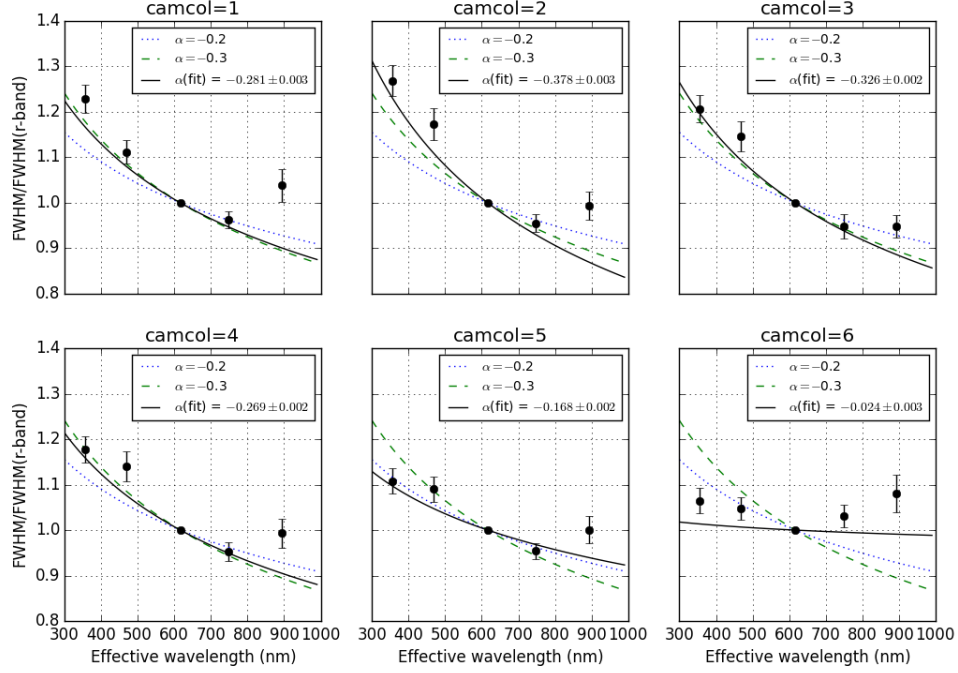


Fig. 3.— The behavior of FWHM as a function of wavelength for the fiducial run 4874. Symbols are SDSS data and solid line is the best power-law fit, with the best-fit slope (α) shown in inset. For comparison purposes, the $\alpha = -0.2$ (dotted) and $\alpha = -0.3$ (dashed) lines are also shown. For the ensemble behavior of best-fit α , see Fig. 4.

data clearly deviate from the Kolmogorov model prediction, which is the horizontal line at $\alpha = -0.20$, with infinite L_0 . For example, for LSST’s fiducial FWHM of 0.6 arcsec and the commonly assumed $L_0 = 30$ m, the von Kármán model predicts an α value close to -0.31 .

4.2. Angular structure function

To examine the angular (spatial) correlation of the FWHM, we compute the angular structure function using PSF measurements from all 6 camera columns. Our structure function is defined as the root-mean-square scatter of the PSF size differences of pairs of stars in the same angular bin³. The SDSS curves are combined for 86 out of the 108 Stripe

³The adopted form of the structure function, SF , is closely related to the autocorrelation function, ACF , as $SF \propto (1 - ACF)^{1/2}$.

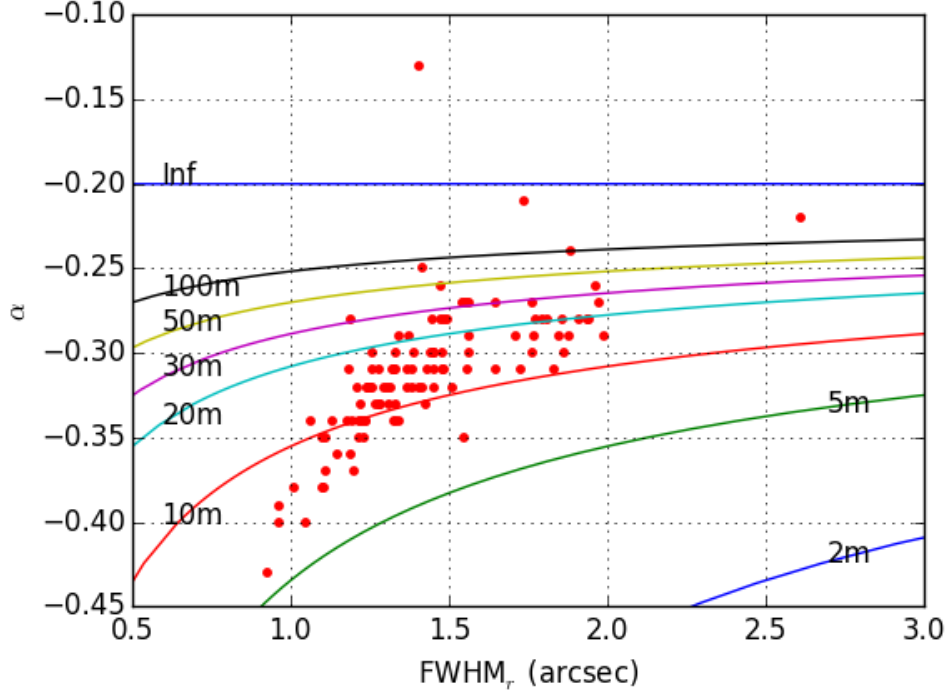


Fig. 4.— The variation of the best-fit power-law index for the wavelength dependence of FWHM, α , vs. the FWHM in the r -band for all the 108 Stripe 82 runs. The symbols are SDSS measurements averaged over all 6 camera columns. The curves are predictions of the von Kármán model, with L_0 ranging from 2 meters to infinity, as labeled. The data are clearly inconsistent with Kolmogorov predictions ($L_0 = \infty$) and reasonably well described by von Kármán model and L_0 in the range from 10m to 30m.

82 runs with the number of fields larger than 100, and then combined for all the bands. We also compared the structure functions for each band separately, and found no statistically significant differences. Results are shown in Fig. 5.

The structure function starts saturating at separations of $\sim 0.5 - 1.0$ degree, with an asymptotic value of about ~ 0.05 arcsec. In other words, the seeing rms variation at large angular scales is about 5%, but we emphasize that our data do not probe scales beyond 2.5 degree.

For comparison, Fig. 5 also shows simulated PSF angular structure functions obtained using PhoSim (Peterson et al. 2015), and results from the CFHT PSF measurements (Heymans et al. 2012). The PhoSim PSF profiles are obtained by simulating a grid of stars spaced by 6 arcminutes with non-perturbed LSST telescope and ideal sensors. The results are aver-

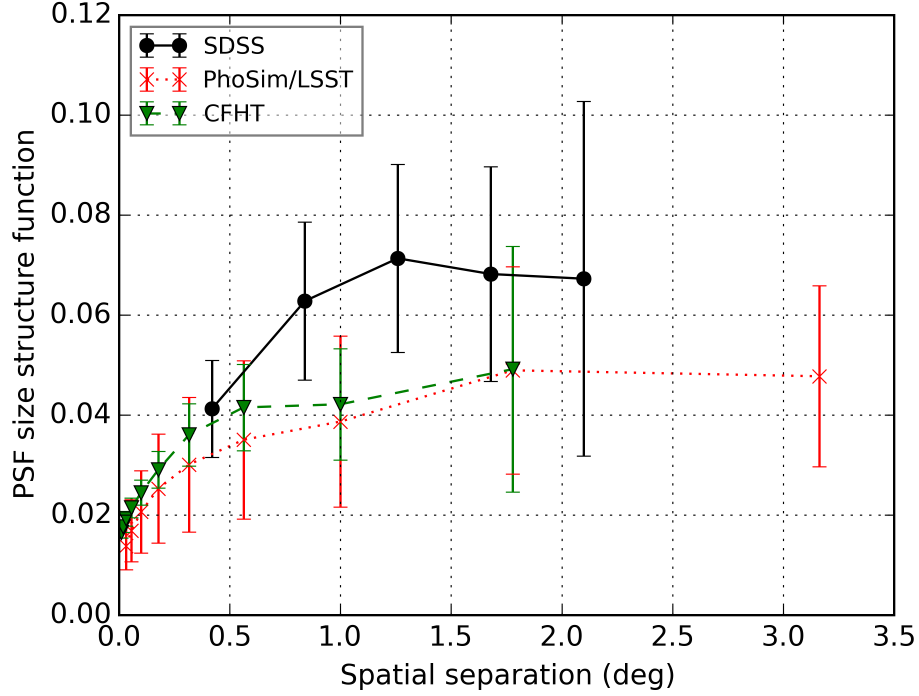


Fig. 5.— The angular structure function for the PSF size determined using CFHT data from Heymans et al. (2012), SDSS data analyzed here, and LSST image simulations. SDSS measurements are averaged over 86 runs with number of fields larger than 100.

aged over 9 different atmosphere realizations with different wind and screen parameters and airmass, and over 3 different wavelengths (350 nm, 660 nm, and 970 nm). The CFHT PSF size measurements were made in the *i*-band, and provided by the authors of Heymans et al. (2012). The three curves in Fig. 5 appear to be quantitatively consistent with each other, even though they correspond to telescopes at different sites and with different optics.

4.3. Temporal behavior

4.3.1. Power spectrum analysis

To study the temporal behavior of the seeing, we first analyze its power spectrum. Fig. 6 shows the temporal power spectral density (PSD) of the PSF FWHM for 6 camera columns, in run 4874, *r*-band. The time difference between subsequent fields is 36 seconds. We fit the PSD using two competing models. The first is a damped random walk (DRW) model (for

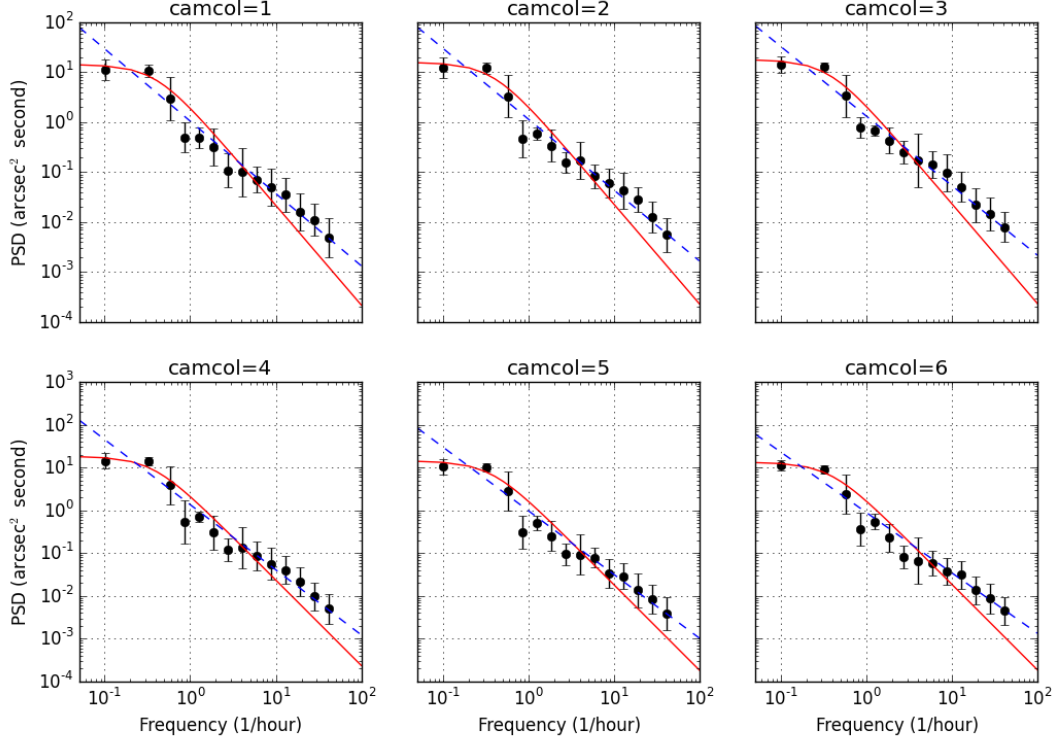


Fig. 6.— PSF size temporal power spectral density for run 4874, r-band. The solid lines are fits using the damped random walk model. The dashed lines show best fits based on a single power law. The former predicts a steeper high-frequency behavior, while the latter cannot explain the turnover at low frequencies.

introduction see Chapter 10 in Ivezić et al. 2014),

$$\text{PSD}(f) = \frac{\tau^2 S F_\infty^2}{1 + (2\pi f \tau)^2}, \quad (8)$$

where f is the temporal frequency, $S F_\infty$ is the asymptotic value of the structure function, and τ is the characteristic timescale. The solid curves in Fig. 6 show fits using this model. Note that due to the lack of data toward the low-frequency end, the first and second bins are four and two times wider than the rest of the bins, respectively. Combining fit results for all camera columns and optical bands for run 4874 gives $\tau = 23.6 \pm 1.3$ minutes. Making the same fits for all the 108 runs in Stripe 82, we obtain the τ distribution vs. the duration of each run, as shown in Fig. 7 (left). The shorter runs tend to give smaller timescale. It is plausible that short runs cannot reliably constrain τ due to the lack of data toward the low-frequency end of the spectra. There are 12 runs longer than 6 hours and their characteristic timescales are within the range of about $\sim 10 - 30$ minutes. This results is generally consistent with

Racine (1996), where a timescale of $\tau = 17 \pm 1$ minutes was found.

The data consistently show a shallower high-frequency behavior than predicted by damped random walk ($\propto 1/f^2$). In order to quantitatively describe the high-frequency tail of the PSD, we fit a simple power law,

$$\text{PSD}(f) = Bf^\beta, \quad (9)$$

where B is the normalization factor, and β is the power-law index. Best-fits are illustrated for run 4874 are in Fig. 6 (dashed lines). Combining fit results for all camera columns and filters gives $\beta = -1.29 \pm 0.09$ for run 4874. Making the same fits for all the 108 runs in Stripe 82, we obtained the β distribution vs. the duration of each run shown in Fig. 7 (right). The shorter runs give β values with a larger variance, but nevertheless it is clear that for most runs the high-frequency behavior can be described with a power-law index in the range -1.5 to -1.0 . On the other hand, a single power law cannot explain the turnover at low frequencies.

Therefore, neither model provides a satisfactory fit over the entire frequency range: the power law fit systematically over predicts the low-frequency part of the PSD, while the $1/f^2$ high-frequency behavior of damped random walk model is too steep. It is likely that a hybrid model would work, but we leave detailed analysis for future work.

4.3.2. Structure function analysis

An alternative approach to power spectrum analysis is offered by auto-correlation and structure function analysis. Following Racine (1996), we define a structure-function-like quantity

$$f(\Delta t) = \frac{|\theta(t + \Delta t) - \theta(t)|}{\theta(t + \Delta t) + \theta(t)}, \quad (10)$$

where θ is seeing. We then fit the mean value of $f(\Delta t)$ to

$$\langle f(\Delta t) \rangle = f(\Delta t)^\infty [1 - \exp(-\Delta t/\tau)^\gamma], \quad (11)$$

with $f(\Delta t)^\infty$, τ and γ as free parameters. Fig. 8 (left) shows one example of such fits. This functional form is somewhat inspired by damped random walk model, where $\gamma = 1$ and the term in brackets is raised to the power of a half. For illustration, Fig. 8 also shows a damped random walk model fit with the same $f(\Delta t)^\infty$ and τ .

The best-fit γ is found to be mostly in the range 1.0 -1.5. The distribution of τ vs. the duration of each run is shown in Fig. 8 (right) (somewhat arbitrarily, we set τ to zero for runs

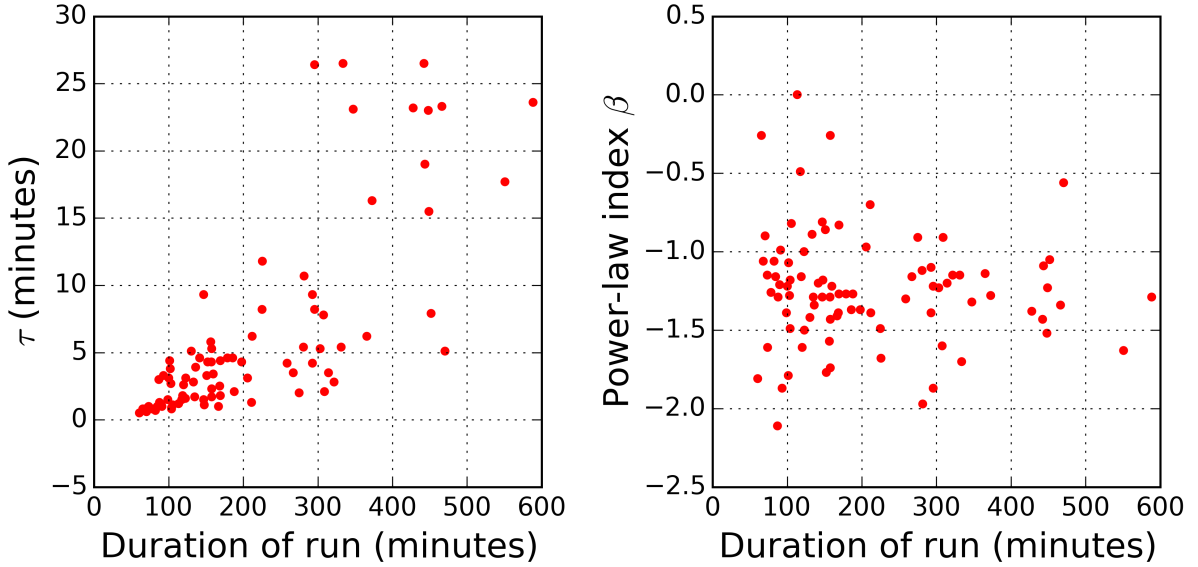


Fig. 7.— Left: The symbols show the best-fit characteristic timescale τ in damped random walk for all 108 runs in Stripe 82 vs. the duration of each run. It is plausible that short runs cannot reliably constrain τ . Right: The power-law index β for a single power law fit for all 108 runs vs. the duration of each run. Note that for the majority of runs, β is larger than the value appropriate for damped random walk ($\beta = -2$).

shorter than 20 minutes). While the short runs show a larger variance in τ , it is evident that for most runs the timescale τ is in the range 10-30 minutes. Therefore, this analysis seems more robust at constraining the characteristic time scale than fitting a damped random walk model to empirical PSD.

5. Discussion and Conclusions

The atmospheric seeing due to atmospheric turbulence plays a major role in ground-based astronomy; seeing varies with the wavelength of observation and with time, on time scales ranging from minutes to years. Better empirical and theoretical understanding of the seeing behavior can inform optimization of large survey programs, such as LSST. We have utilized here for the first time an unprecedentedly large database of about a million SDSS seeing estimates and studied the seeing profile and its behavior as a function of time and wavelength.

We find that the observed PSF profile can be parametrized by only two parameters, the FWHM of a theoretically motivated profile and a normalization of the contribution of an

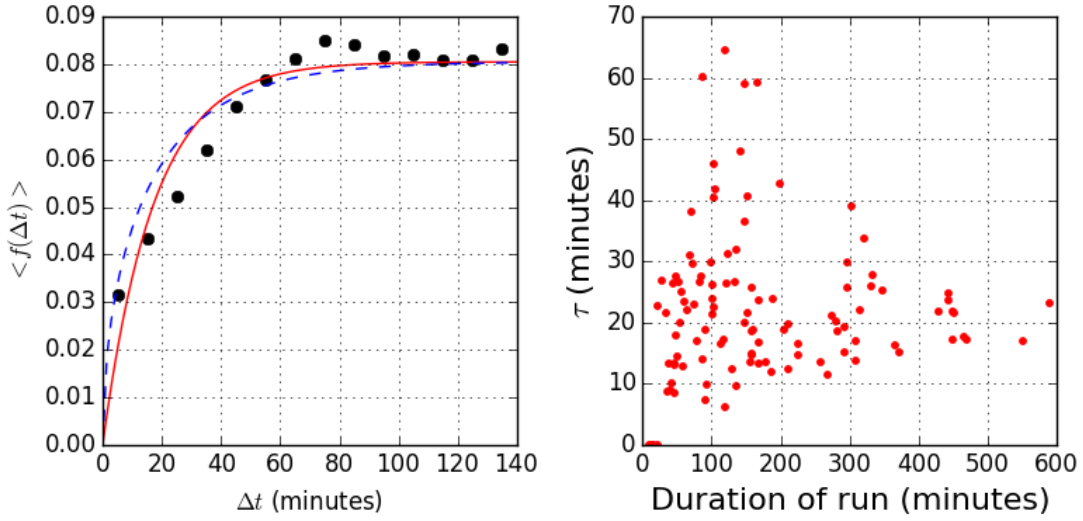


Fig. 8.— Left: The average normalized seeing difference, $\langle f(\Delta t) \rangle$, as a function of the time separation, Δt , for run 4874, camera column 1, in the r -band. The fit to Eq. (11) gives $f(\Delta t)^\infty = 0.08$, $\tau = 25.9$ minutes and $\gamma = 1.49$. The dashed line is the structure function predicted by damped random walk model with the same $f(\Delta t)^\infty$ and τ . Right: The timescale τ for all 108 runs vs. the duration of each run. Note that for most runs τ is in the range 10-30 minutes (τ is set to zero for runs shorter than 20 minutes).

empirically determined instrumental PSF. The profile shape is very similar to the “double gaussian plus power-law wing” decomposition used by SDSS image processing pipeline, but here it is modeled with two free model parameters, rather than six as in SDSS pipeline (of course, the SDSS image processing pipeline had to be designed with adequate flexibility to be able to efficiently and robustly handle various unanticipated behavior). We find that the PSF profile is well described by theoretical predictions based on both Kolmogorov and von Kármán’s turbulence theory (see Fig. 2). Given the extra degree of freedom due to the instrumental PSF, the shape of the measured profile alone is insufficient to reliably rule out either of the two theoretical profiles.

We report empirical evidence that the wavelength dependence of the atmospheric seeing and its correlation with the seeing itself agrees better with the von Kármán model than the Kolmogorov turbulence theory (see Fig. 4). For example, the best-fit power-law index to describe the seeing wavelength dependence in conditions representative for LSST survey is much closer to -0.3 than to the usually assumed value of -0.2 predicted by the Kolmogorov theory. We note that most of the long-term seeing statistics are measured at visible wavelengths. The knowledge of the wavelength-dependence of the seeing is useful for extrap-

olating the seeing statistics to other wavelengths, for example, to the near-infrared where a lot of the adaptive optics programs operate.

We have also measured the characteristic angular and temporal scales on which the seeing decorrelates. The angular structure function saturates at scales beyond 0.5–1.0 degree. The seeing rms variation at large angular scales is about 5%, but we emphasize that our data do not probe scales beyond 2.5 degree. Comparisons with simulations of the LSST and PSF measurements at the CFHT site show good general agreement.

The power spectrum of the temporal behavior is found to be broadly consistent with a damped random walk model with characteristic timescale in the range $\sim 10 - 30$ minutes, though data show a shallower high-frequency behavior. The high-frequency behavior can be quantitatively described by a single power law with index in the range -1.5 to -1.0 . A hybrid model is likely needed to fully capture both the low-frequency and high-frequency behavior of the temporal variations of atmospheric seeing.

We conclude by noting that, while our numerical results may only apply to the SDSS site, they can be used as useful reference points when considering spatial and temporal variations of seeing at other observatories.

This material is based upon work supported in part by the National Science Foundation through Cooperative Agreement 1258333 managed by the Association of Universities for Research in Astronomy (AURA), and the Department of Energy under Contract No. DE-AC02-76SF00515 with the SLAC National Accelerator Laboratory. Additional LSST funding comes from private donations, grants to universities, and in-kind support from LSSTC Institutional Members.

Funding for the SDSS and SDSS-II has been provided by the Alfred P. Sloan Foundation, the Participating Institutions, the National Science Foundation, the U.S. Department of Energy, the National Aeronautics and Space Administration, the Japanese Monbukagakusho, the Max Planck Society, and the Higher Education Funding Council for England. The SDSS Web Site is <http://www.sdss.org/>.

REFERENCES

- Boccas, M. 2004, Gemini Technical Note
- Borgnino, J. 1990, *Appl. Opt.*, 29, 1863
- Gunn, J. E., et al. 2006, *AJ*, 131, 2332

- Heymans, C., Rowe, B., Hoekstra, H., Miller, L., Erben, T., Kitching, T., & van Waerbeke, L. 2012, MNRAS, 421, 381
- Ivezić, Ž., Connolly, A. J., VanderPlas, J. T., & Gray, A. 2014, Statistics, Data Mining, and Machine Learning in Astronomy
- Ivezić, Ž., et al. 2007, AJ, 134, 973
- Ivezić, Ž., et al. 2008, arXiv:0805.2366v4
- Lupton, R., Gunn, J. E., Ivezić, Ž., Knapp, G. R., & Kent, S. 2001, in Astronomical Society of the Pacific Conference Series, Vol. 238, Astronomical Data Analysis Software and Systems X, ed. F. R. Harnden, Jr., F. A. Primini, & H. E. Payne, 269
- Lupton, R. H., Ivezić, Ž., Gunn, J. E., Knapp, G., Strauss, M. A., & Yasuda, N. 2002, in Society of Photo-Optical Instrumentation Engineers (SPIE) Conference Series, Vol. 4836, Survey and Other Telescope Technologies and Discoveries, ed. J. A. Tyson & S. Wolff, 350
- Martinez, P., Kolb, J., Sarazin, M., & Tokovinin, A. 2010, The Messenger, 141, 5
- Oya, S., Terada, H., Hayano, Y., Watanabe, M., Hattori, M., & Minowa, Y. 2016, Experimental Astronomy, 42, 85
- Peterson et al., J. R. 2015, ApJS, 218, 14
- Pier, J. R., Munn, J. A., Hindsley, R. B., Hennessy, G. S., Kent, S. M., Lupton, R. H., & Ivezić, Ž. 2003, AJ, 125, 1559
- Racine, R. 1996, PASP, 108, 372
- Racine, R. 2009, in Optical Turbulence: Astronomy Meets Meteorology, ed. E. Masciadri & M. Sarazin, 13
- Roddier, F. 1981, Progress in optics. Volume 19. Amsterdam, North-Holland Publishing Co., 1981, p. 281-376., 19, 281
- Sesar, B., et al. 2007, AJ, 134, 2236
- Stoughton, C., et al. 2002, AJ, 123, 485
- Tokovinin, A. 2002, PASP, 114, 1156
- Vernin, J., & Muñoz-Tuñón, C. 1998, New A Rev., 42, 451

York, D. G., et al. 2000, *AJ*, 120, 1579

Ziad, A., Conan, R., Tokovinin, A., Martin, F., & Borgnino, J. 2000, *Appl. Opt.*, 39, 5415